

Plane-wave compounding with adaptive joint coherence factor weighting

Nikunj Khetan, Jerome Mertz

Abstract—Coherent Plane Wave Compounding (CPWC) is widely used for ultrasound imaging. This technique involves sending plane waves into a sample at different transmit angles and recording the resultant backscattered echo at different receive positions. The time-delayed signals from the different combinations of transmit angles and receive positions are then coherently summed to produce a beamformed image. Various techniques have been developed to characterize the quality of CPWC beamforming based on the measured coherence across the transmit or receive apertures. Here, we propose a more fine-grained approach where the signals from every transmit/receive combination are separately evaluated using a quality metric based on their joint spatio-angular coherence. The signals are then individually weighted according to their measured Joint Coherence Factor (JCF) prior to being coherently summed. To facilitate the comparison of JCF beamforming compared to alternative techniques, we further propose a method of image display standardization based on contrast matching. We show results from tissue-mimicking phantoms and human soft-tissue imaging. Fine-grained JCF weighting is found to improve CPWC image quality compared to alternative approaches.

I. INTRODUCTION

Ultrasound imaging is widely used in modern healthcare because it is non-invasive, low cost and broadly applicable. In most cases, ultrasound image reconstruction is based on the line-by-line application of a simple delay-and-sum (DAS) algorithm to the received echo signals, limiting imaging speeds to roughly video rate. However, the introduction of coherent plane wave compounding (CPWC) [1] has led to a huge advance in the field by enabling unprecedented speeds with little compromise in image quality. Already, CPWC is used in a variety of clinical applications, such as shear wave imaging [1] and Doppler-based flow imaging [2].

However, CPWC is not without its limitations. Because it is a multiplexing technique, it is generally more susceptible to noise than line-by-line techniques making use of focused transmit beams. Several sources of noise can degrade signal in CPWC, such as off-axis or out-of-focus clutter, deviations in the local speed of sound caused by sample inhomogeneities, multiple scattering within the sample or from subresolution features resulting in speckle noise, uncorrelated electronic noise, etc.. In addition, because CPWC requires data obtained from several successive plane-wave insonifications, any inter-

frame micro-motion within the sample, random or otherwise, can induce error in the CPWC reconstruction.

A key advance in the implementation of CPWC has been the recognition that not all signals are of high quality. This has led to the formulation of a variety of metrics to characterize signal quality, which can then be used to adaptively optimize the reconstruction of images based on the incoming signals themselves. A common metric is the coherence factor [3], which measures the self-similarity of signals across a particular dimension. A high degree of self-similarity, or correlation, is indicative of high-quality signal whereas a low degree is indicative of noise or clutter, which is to be suppressed.

Early approaches in ultrasound imaging adopted the concept of a spatial coherence factor (CF) [4], wherein self-similarity is measured along the dimension of the receive aperture space. In this case, the CF is defined as the ratio of coherent to incoherent signal power across the aperture transducer elements. While initially the spatial CF was used simply to characterize image quality, it was quickly realized that it could be applied as a filter to adaptively suppress uncorrelated noise or clutter [5]. Successive variations of the CF came to being. For example, the generalized CF (GCF) is a metric based on the spatial frequency content of the signal, given by the ratio of the signal power below a cutoff frequency to the total power [6]. Alternatively, the phase coherence factor (PCF) is a measure of the phase variations across the aperture [7].

While the spatial CF is essentially a measure of the normalized variance of signal strengths across the receive aperture [8], more comprehensive information is provided by signal covariance. For example, the short lag spatial coherence (SLSC) [9], [10] provides a measure of the signal covariance strength up to a cutoff lag, where a short cutoff lag plays a similar role as a high cutoff frequency in GCF. The delay multiply and sum (DMAS) algorithm [11], provides a measure of covariance strength over all lags, making it similar to SLSC (though normalized differently and without an added step of local time averaging). Different from CF approaches, SLSC and DMAS generally provide final images rather than serving as filter-functions that are subsequently applied to DAS-based image reconstruction.

More recently, it has been recognized that coherence in the receive aperture can equally be applied to coherence in the transmit aperture, owing to the principle of acoustic reciprocity [12]. When applied to CPWC, this led to the concept of short lag angular coherence (SLAC) [12], which is the analog of SLSC but with covariance measured along the transmit coordinate (angle) rather than the receive coordinate (space). It has also led to the concept of an angular CF, and

This work was partially supported by the National Institutes of Health (R21GM134216) and by the Boston University Photonics Center.

N. K. is with Boston University Mechanical Engineering, 110 Cummington Mall, Boston, MA 02215 (e-mail: nkhetan@bu.edu).

J. M. is with Boston University Biomedical Engineering, 44 Cummington Mall, Boston, MA 02215 (e-mail: jmertz@bu.edu).

ultimately to the concept of a united CF (UCF) [13] that aims to combine signal variance information along both angle and space coordinates. However, as will be shown below, UCF does not fully exploit this information.

Of course, other filtering strategies are possible. Notably, the Capon minimum variance (MinVar) algorithm derives the filter weights that optimally suppress clutter noise while preserving signal gain [14]. Indeed, efforts have been made to apply MinVar weighting across both spatial and angular coordinates [15]–[17], though with a drawback that MinVar weights are derived according to expectations of signal covariances. These expectations must be estimated from the actual measured signal covariances, often requiring signal pooling that can undermine the benefits of MinVar weighting in the first place. In general, the MinVar algorithm must be applied with care, since small errors in the expected covariances can easily lead to worse outcomes in image quality.

In this work, we re-examine the application of CF-based filtering to CPWC. We propose a new filtering algorithm that is inspired by previous CF methods but goes a step further in how fine-grained the level of filtering is taken. Rather than consider a spatial or angular CF separately, or try to amalgamate these into a single weighting factor [13], we consider every possible combination of transmit to receive sound trajectories. Our premise is that different trajectories yield different signal qualities depending on the different uncontrollable influences they are subjected to (clutter, inhomogeneities, scattering, noise, etc.). That is, to each transmit/receive trajectory we assign a quality metric specific to that trajectory, based on the measured signals themselves. By suppressing the low quality signals at the fine-grained level of each individual trajectory, we thus suppress their deleterious contributions.

This paper is organized as follows. In section 2, we describe how the individual trajectory weights are calculated based on the measured signals, using an adaptive joint coherence factor (JCF) algorithm applied to CPWC. We also introduce a method of contrast matching to standardize the comparison between images. In section 3, we compare the results of JCF weighting with other popular weighting strategies, using datasets collected from both phantom and human imaging. As will be shown, JCF weighting compares favorably to other strategies.

II. THEORY AND METHODS

We consider here a linear transducer array of N elements with position x_n along the azimuthal direction. CPWC is performed by transmitting a set of M plane waves into the sample, each with different steering angle θ_m . The resulting echo signals associated with any given target location (x, z) within the sample, appropriately time delayed, are thus obtained in the form of a $M \times N$ matrix, with element $s_{m,n}$ corresponding to the signal obtained from a plane wave transmit of steering angle θ_m and received on array element x_n :

$$\mathbf{S}(x, z) = \begin{bmatrix} s_{1,1} & s_{1,2} & \dots & s_{1,N} \\ s_{2,1} & s_{2,2} & \dots & s_{2,N} \\ \dots & \dots & \dots & \dots \\ s_{M,1} & s_{M,2} & \dots & s_{M,N} \end{bmatrix} \quad (1)$$

That is, $\mathbf{S}(x, z)$ encompasses the signal elements obtained from every combination of transmit angles and receive positions, corresponding to different sound trajectories. We assume these signals are complex (i.e. they are the complex analytical representations of the measured real signals), and henceforth omit the dependence of \mathbf{S} on (x, z) , taking this to be implicit.

A. Beamforming with JCF weighting

In the conventional DAS implementation of CPWC, the beamformed field associated with a sample target location is given by the simple summation of the signal elements in \mathbf{S} (possibly weighted by fixed apodization factors, which we omit for brevity). That is,

$$B_{DAS}(x, z) = \frac{1}{MN} \sum_{m=1}^M \sum_{n=1}^N s_{m,n} \quad (2)$$

Our basic strategy is not to treat each signal element $s_{m,n}$ equally, as in standard DAS beamforming, but rather to adaptively assign a weighting factor $w_{m,n}$ to each signal element based on their measured quality. That is, our beamforming is given by

$$B_{JCF}(x, z) = \frac{1}{MN} \sum_{m=1}^M \sum_{n=1}^N w_{m,n} s_{m,n} \quad (3)$$

The metric we use here to define signal quality is based on a joint spatio-angular coherence factor (JCF for short), defined by

$$w_{m,n}(x, z) = \frac{\left| \sum_{m'=1}^M \sum_{n'=1}^N s_{m',n} s_{m,n'} \right|^\alpha}{(MN)^{\alpha-1} \sum_{m'=1}^M \sum_{n'=1}^N |s_{m',n}|^\alpha |s_{m,n'}|^\alpha} \quad (4)$$

where $\alpha \geq 0$ is a user-defined ‘‘smoothness’’ parameter whose role will be made clear later (note that JCF beamforming reduces to conventional DAS beamforming when $\alpha = 0$). Equation (4) has a simple interpretation: $w_{m,n}$ corresponds to the coherence of $s_{m,n}$ measured jointly along both the spatial (associated row) and angular (associated column) directions. $w_{m,n}$ ranges between 0 and 1, indicating low and high degrees of coherence respectively. Signal elements with low coherence are considered corrupted and of low quality, and suppressed accordingly. We emphasize here that $w_{m,n}$ is a two dimensional matrix, as opposed to the weighting factors used in most filtering-based techniques which are one dimensional vectors, or scalar in UCF (see Tables I and II). In other words, $w_{m,n}$ weights each signal element individually, as opposed to weighting entire rows or columns of signal elements, or the entire matrix of signal elements. As will be shown below, this leads to considerable improvements in image quality.

B. Contrast matching

To properly assess the benefits of JCF beamforming compared to alternative methods, we must first standardize what we mean by image quality. Common definitions of image quality involve the association of a contrast ratio (CR) [18]

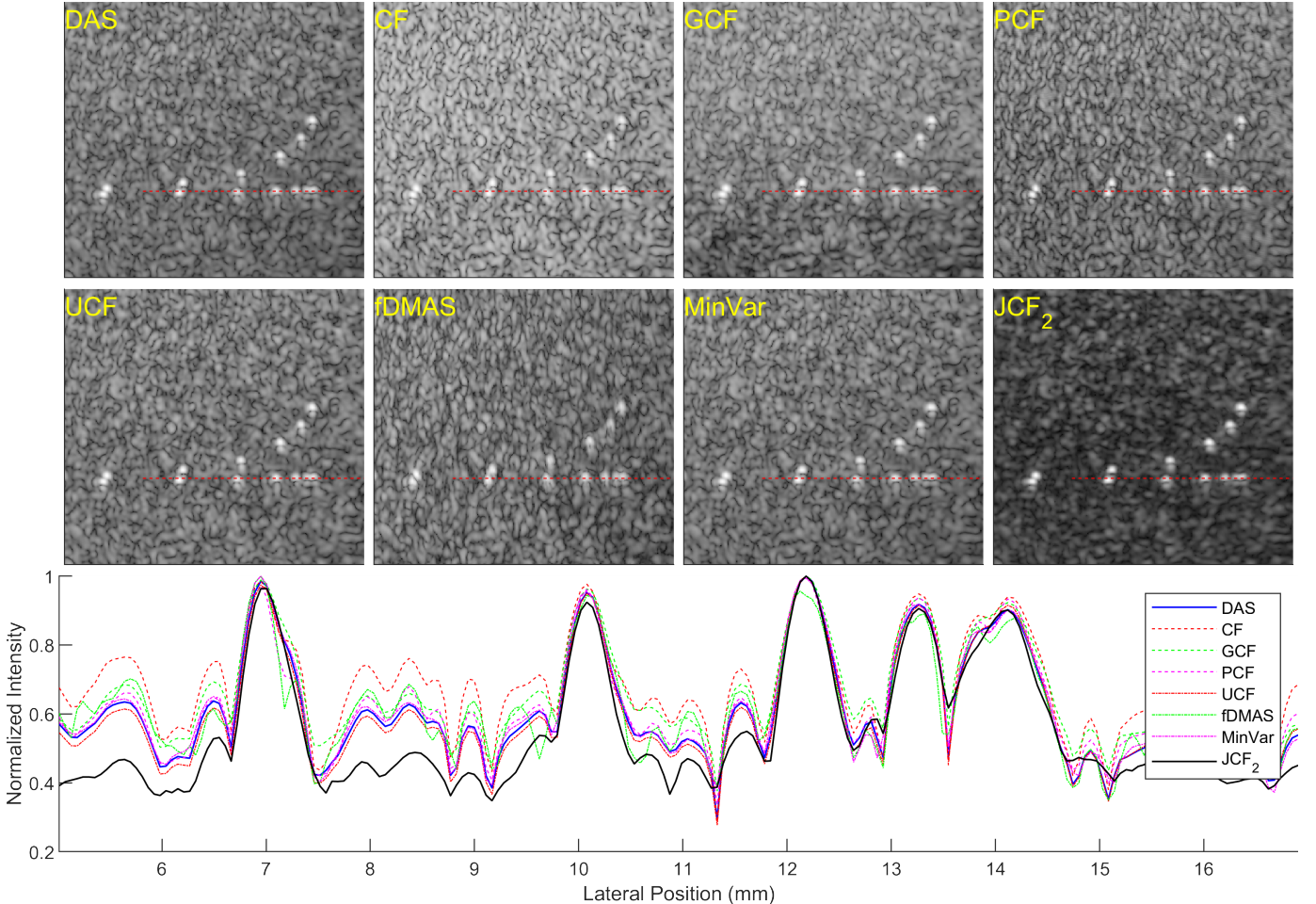


Fig. 1. Top: Contrast-matched images of resolution targets in a CIRS GSE 040 phantom obtained at 30 mm depth. Beamforming reconstruction method is indicated in panels, where JCF_2 indicates $\alpha = 2$. Image size is 16 mm x 15 mm (Horizontal x Vertical). Bottom: Intensity plots across red lines in panels. JCF suppresses speckle noise without noticeably affecting resolution.

or a contrast-to-noise ratio (CNR) [19] to the image. These definitions compare signal with background (or background noise), meaning they require an a priori delineation between what is understood to be signal and what is understood to be background. When imaging phantom samples of known inclusions, such a delineation is clear; however, when imaging samples with unknown inclusions where the distinction between signal and background is not so clear cut this delineation becomes decidedly less straightforward. Exacerbating this difficulty is the problem that ultrasound signals can span an enormously large dynamic range, meaning that some form of intensity compression is required for the display of images. The simplest and most common approaches involve log or gamma compression, though more sophisticated approaches can also be applied [20], [21]. However, it is well known that both CR and CNR vary considerably with different compression algorithms, meaning they are not reliable indicators of image quality to start with. This has led to the formulation of a generalized CNR (gCNR) [22] which characterizes the separability between signal and background in a compression-agnostic manner. However, the gCNR metric requires yet additional a priori information, not only about the binary

distinction between signal and background, but also about the respective intensity statistics of each. Such information, again, is difficult if not impossible to obtain when imaging real samples. In other words, a quantitative metric for ultrasound image quality has proven surprisingly difficult to define [23].

In this work, we fully acknowledge this difficulty. Nevertheless, our aim is to provide side-by-side comparisons of images obtained with different beamforming methods. To ensure (as best we can) that these comparisons are made with images on equal footing, we introduce here a strategy of contrast matching wherein the contrasts of all images are adjusted to be the same upon display. In particular, we choose the contrast of the DAS image to serve as the reference contrast. In our case, the DAS image is displayed with commonly used gamma compression, using a gamma factor set here to $\gamma_{DAS} = 0.25$. That is, throughout this work DAS images are displayed with pixel values given by

$$I_{DAS}(x, z) = |B_{DAS}(x, z)|^{\gamma_{DAS}=0.25} \quad (5)$$

We define the contrast of this DAS image to be [24]

$$K_{DAS} = \frac{\sigma_{DAS}}{\langle I_{DAS} \rangle} \quad (6)$$

where $\langle I_{DAS} \rangle$ and σ_{DAS} correspond respectively to the mean and standard deviation of the pixel values across the displayed image. That is, K_{DAS} is a measure of the relative range of pixel variations throughout the displayed DAS image. This measure has the advantage that it makes no attempt to categorize pixels as belonging to signal or background, and thus requires no a priori information. All images generated by alternative beamforming methods are then adjusted, also by gamma compression, so that their displayed contrast matches that of the reference DAS image. As an example, let us consider an image obtained with JCF beamforming. The displayed JCF image is given by

$$I_{JCF}(x, z) = |B_{JCF}(x, z)|^{\gamma_{JCF}} \quad (7)$$

where the gamma factor γ_{JCF} is chosen such that $K_{JCF} = K_{DAS}$, and so forth for other beamforming methods. In this manner, images from different methods are compared under the constraint that their relative pixel variations are kept the same. While this method of contrast matching fails to provide a quantitative image quality metric, it does facilitate the comparison of images by providing some degree of standardization between them.

C. Experiments

Results presented in this paper were generated by data obtained either experimentally or from an online repository. Experimental data was obtained using a Verasonics Vantage 256 system. Data processing was performed in Matlab. We wrote a custom C++ beamformer using the open-source Eigen library [25] inspired by the approach presented in the Matlab Ultrasound Toolbox (MUST) [26], [27]. We also implemented most of the algorithms described in Tables I and II using C++ and Eigen, according to similar Matlab implementations from the Ultrasound Toolbox [28]. All displayed images were compressed according to the contrast matching procedure described above, for standardized comparison. A sample Matlab implementation is available at https://github.com/biomechanics/Ultrasound_JCF.

III. RESULTS

To begin, we imaged resolution point targets in a standard tissue-mimicking phantom (CIRS 040GSE Multi-Purpose Multi-Tissue Ultrasound Phantom) using a GE9LD probe (192 elements, element size 0.23 mm, center frequency 5.2 MHz). CPWC data was obtained using a sequence of 75 plane waves of angles θ uniformly distributed from -24 To 24 degrees. The results comparing several different beamforming modalities are shown in Fig. 1, where JCF₂ indicates α was set to 2. Plots of the displayed intensities across the indicated red lines are shown in the bottom panel. Several takeaways can be inferred from this plot. The first is that all the filtering techniques presented here produce more or less similar results compared to DAS in terms of target resolution (peak widths) and linearity (peak heights across the plots). However, when comparing the background noise throughout the images, we find that JCF₂ provides a consistently lower and smoother baseline than the other techniques. The reason for this is that the background

here comes from speckle noise resulting from sub-resolution scatterers. Because the scatterers are distributed randomly within each resolution volume, each transmit/receive combination produces a randomly varying signal element $s_{m,n}$ bearing little coherence relative to neighboring signal elements. When summed coherently, the signal elements produce highly noisy speckle of amplitude distribution defined by Rayleigh statistics [24]. JCF effectively attenuates such weakly coherent noise, manifestly more so than other techniques.

Figure 2 shows the results from an open-source CPWC dataset of a carotid artery from the PICMUS challenge [29]. Here we include different JCF variants where α ranges from 1 to 4. We emphasize that the overall contrast of each panel, as defined by Eq. 6, is rigorously kept the same, and yet the contrast of the JCF panels appears higher than the rest (the apparent contrast increasing with α). The reason for this is that JCF filtering suppresses noise and clutter better than the other modalities. As such, the pixels that contribute to contrast in the JCF images are dominantly signal pixels, whereas much of the contrast from the other modalities originates from noise or clutter. An examination of the artery lumen further reveals that the streak artifacts apparent with other modalities all but disappear in the JCF panels, particularly as α increases.

Figure 3 shows images of stomach tissue obtained from a healthy volunteer. Again we used a GE9LD probe, this time with 45 plane-wave transmits of angles uniformly distributed between -10 and 10 degrees. Again, the noise and clutter in the JCF panel appear smoother and more suppressed compared to the rest. This is more apparent when the images are magnified (zoomed region delimited by the red box in the DAS panel).

Figures 4 and 5 show images of calf muscle tissue from the same volunteer, acquired this time with a L12-3v probe (128 elements, element size 0.2 mm, center frequency 9 MHz) using 45 plane-wave transmits of angles uniformly distributed between -18 and 18. Two zoom levels are shown of increasing magnification (red boxes). The benefits of JCF are most apparent at higher magnification (Fig. 5). Whereas the images from all other modalities are marred by considerable speckle noise that masks the underlying sample structure, the JCF panel is largely devoid of this noise. As a result, the sample structure (here perimysial septa [30]) appears much less distorted and mottled. These panels in particular highlight the deficiency in using contrast alone as a measure of image quality. The contrasts of all panels in Fig. 5 are matched to be the same, and yet the image quality provided by JCF appears manifestly better.

Finally, Fig. 6 shows side-by-side comparisons of the effect of increasing the smoothness parameter α , compared to conventional DAS (recalling that DAS is equivalent to JCF₀). The transition from $\alpha = 0$ to $\alpha = 1$ provides the most benefit in image quality. This trend continues with increasing α , though with diminishing returns in imaging quality and noise suppression. Notably, increasing α does not appear to undermine spatial resolution in any way, nor does it appear to alter the relative brightnesses of the signals themselves.

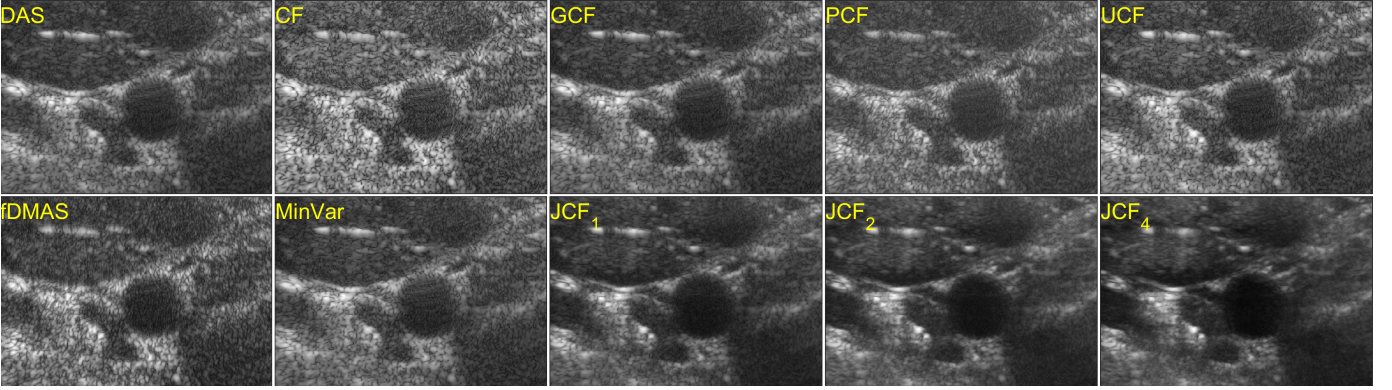


Fig. 2. Contrast-matched images beamformed from open-source raw data of a carotid artery (cross-sectional view) made available through the PICMUS challenge [29]. JCF images are shown with increasing values of the smoothness parameter α , leading to increasing suppression of noise and clutter. Image size is 38 mm x 45 mm (Horizontal x Vertical).

IV. DISCUSSION

The basic principle of JCF is to individually weight every signal element $s_{m,n}$ within the full transmit/receive matrix \mathbf{S} according to its respective signal quality. The weighting $w_{m,n}$ is adaptive in the sense that the signal qualities are derived from the measurements themselves rather than from a predefined model. That is, different combinations of transmit angle (indexed by m) and receive position (indexed by n) can produce different degrees of signal quality based more or less on happenstance, depending on a variety of factors that, in general, cannot be predicted or controlled in advance. Signal quality for each transmit/receive combination (m, n) is determined here by the degree of coherence measured jointly across both the associated transmit angles (column n) and associated receive positions (row m). The jointness of this measure is a defining feature of JCF-assisted CPWC beamforming.

Different factors can affect the measured coherence of each signal element. For example, if measurements are dominated by clutter or electronic noise, then the elements $s_{m,n}$ are dominantly uncorrelated with one another and $w_{m,n}$ becomes correspondingly low. Similarly, if random sample micro-motion occurs between each transmit event, this too leads to row and/or column decorrelation between $s_{m,n}$ elements, also leading to low $w_{m,n}$. Another source of decorrelation can come from upstream sample occlusions or aberrations that can cause changes in amplitude or phase that are different for different (m, n) combinations. Yet another source of decorrelation comes from the presence of randomly distributed sub-resolution scatterers, as discussed related to Fig. 1, leading to speckle noise. Regardless of the sources of decorrelations, their resulting effects on signal quality are considered deleterious. JCF makes no attempt to correct for these effects, but rather suppresses them according to their severity. As a result, the remaining signal elements that contribute to the coherent summation in CPWC feature high degrees of row/column coherence, leading to noticeable improvements in image quality.

The benefits in image quality that we report here are more qualitative than quantitative. The reason for this stems from

the difficulty in defining a quantitative metric for image quality that does not rely on a priori knowledge of the sample. Nevertheless, we established a methodology based on contrast matching to provide a reasonably level field for comparison between different CPWC beamforming modalities. This methodology makes use of gamma compression with gamma values adjusted to yield a consistent predefined image contrast across all modalities. In our case, we chose the DAS image contrast to serve as the predefined reference contrast. For all our results, we purposefully chose a somewhat low γ_{DAS} value of 0.25 to better reveal the weak intensities in our displayed images, where the benefits of JCF are most apparent. A different reference gamma value could, of course, also be used.

Regarding the benefits of JCF, the most significant is the suppression of uncorrelated noise or clutter in the beamformed images, leading to an increase in *apparent* image contrast that better enables the distinction between signal and background, at least qualitatively. JCF uses the same raw data as conventional DAS CPWC, with no requirement of additional measurements or a priori knowledge about the sample. However, the benefits do not come without trade-offs. There is an additional computational load associated with JCF. In our case, there was also an additional requirement of computer memory. Our specific implementation was tailored for post-processing of saved, time-delayed data rather than for real-time processing. This approach involved saving the entire 4D $\mathbf{S}(x, z)$ matrix instead of calculating a 2D \mathbf{S} matrix for each (x, z) sample coordinate on the fly. With our system (Intel Xeon E5-2680 2.5 GHz CPU, 12 cores, 24 threads, 128 GB DDR4 RAM), JCF beamforming was approximately 3-4 times slower than standard DAS beamforming. We anticipate that a more optimized, pixel-wise approach and/or GPU-based implementation could significantly speed up JCF beamforming and enable live imaging applications.

V. CONCLUSION

We have described a method to identify and suppress uncorrelated noise in CPWC beamforming. The method involves a fine-grained adaptive filtering at the level of the individual sig-

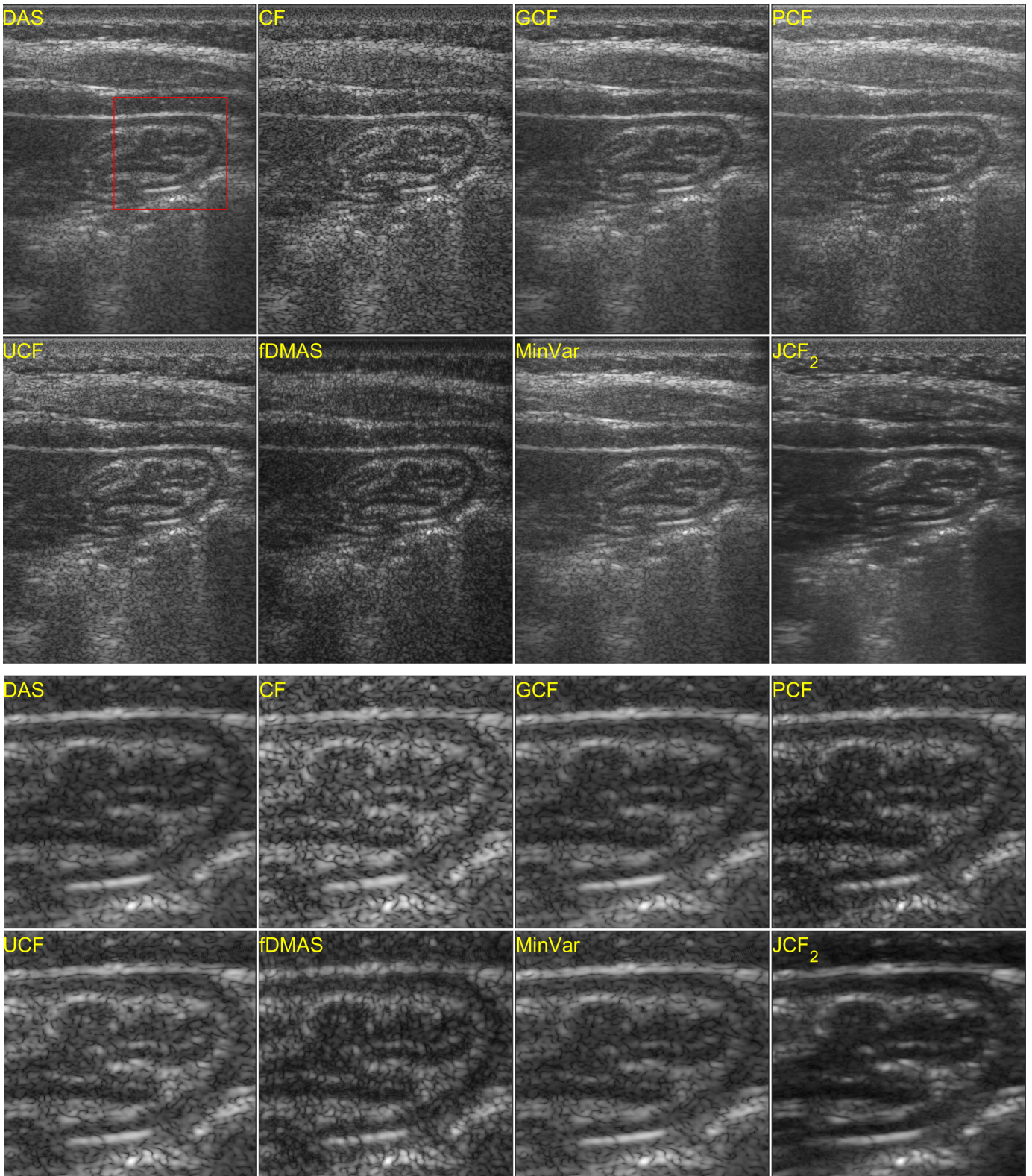


Fig. 3. Top: Contrast-matched images of stomach tissue from a healthy volunteer. Image size is 44 mm x 57 mm (Horizontal x Vertical). Bottom: Contrast-matched images of magnified region indicated by red box in DAS panel above. Image size is 19 mm x 19 mm (Horizontal x Vertical).

nal elements contributing to conventional DAS coherent summation, based on their local spatio-angular joint coherence. The benefits are a reduction and smoothing of background noise and clutter, leading to improved image quality. The

benefits are apparent, for example, when images are corrupted by random patchiness caused by speckle noise, which can severely distort and mask the underlying signals of interest. JCF effectively attenuates this noise without noticeable loss

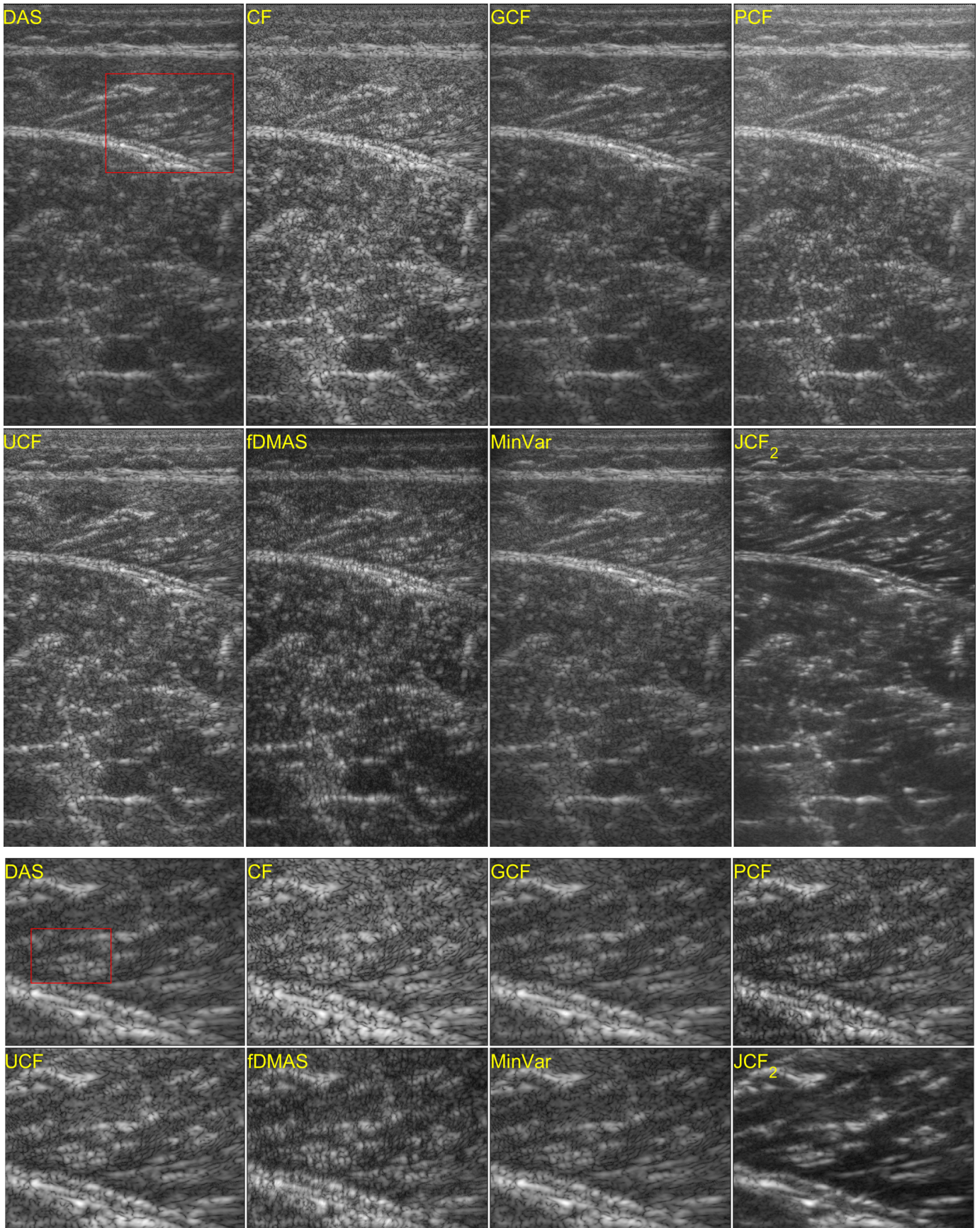


Fig. 4. Top: Contrast-matched images of calf muscle from a healthy volunteer. Image size is 25 mm x 44 mm (Horizontal x Vertical). Bottom: Contrast-matched images of magnified region indicated by red box in DAS panel above. Image size is 13 mm x 10 mm (Horizontal x Vertical).

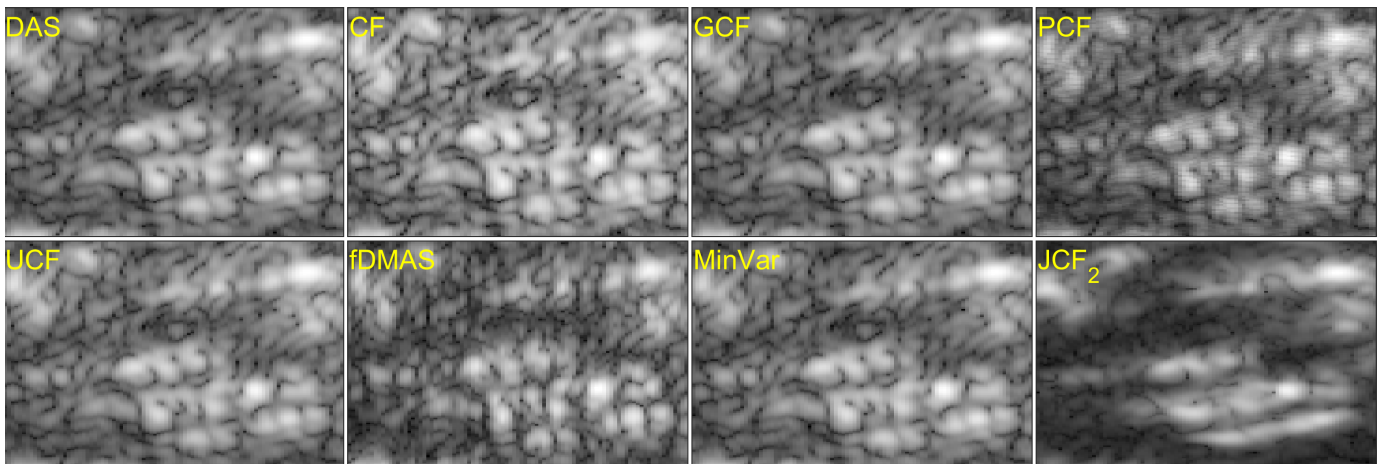


Fig. 5. Continuation of Fig. 4 with increasing magnification of region indicated by red box in DAS panel. All panel sets are contrast-matched to respective DAS panel. JCF suppresses patchiness and distortions caused by speckle noise and clutter. Image size is 5 mm x 3 mm (Horizontal x Vertical).

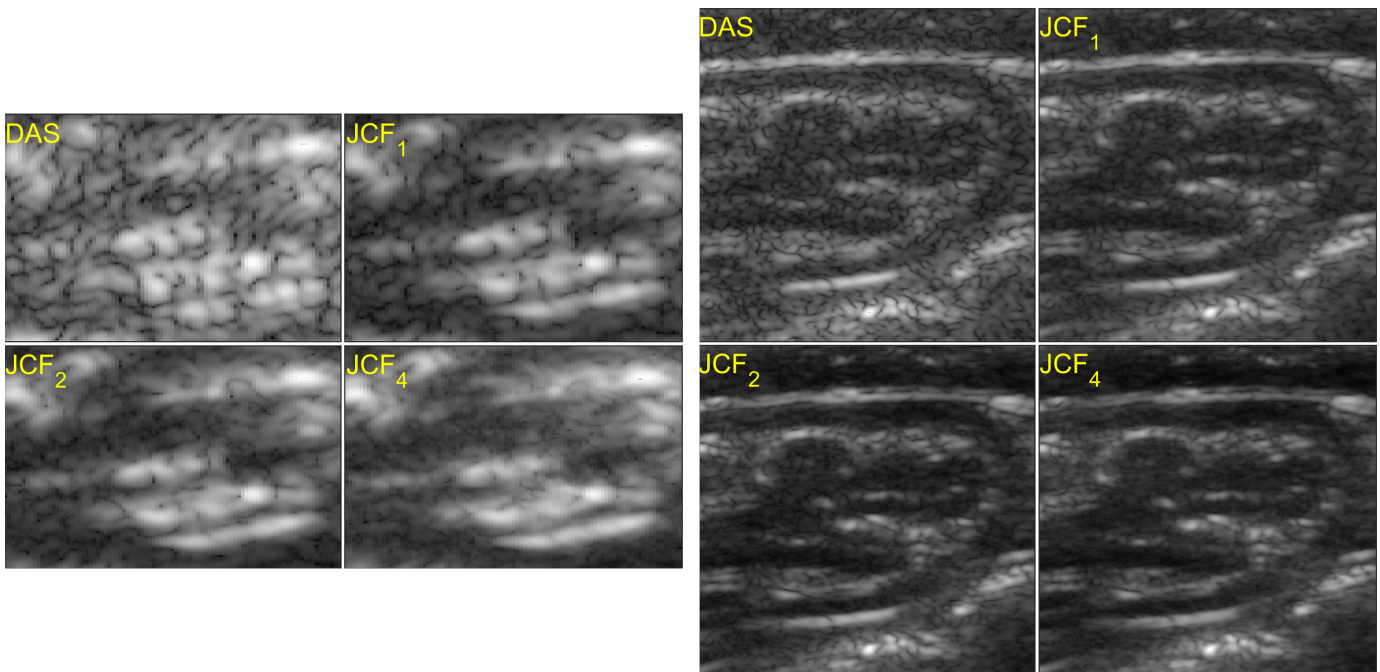


Fig. 6. Effect of change in smoothness parameter α on image quality ($\alpha = 0$ is equivalent to DAS). Left: same view as Fig. 5. Right: same view as Fig. 3, bottom. Panels are contrast-matched. Increasing α increases noise and clutter suppression with little effect on resolution.

in spatial resolution. We further introduced a general contrast-matching approach to facilitate the comparison of JCF with other methods of image filtering. The aim of this work is to add JCF to the arsenal of CPWC beamforming strategies, with the hope of improving ultrasound imaging quality in medical applications.

ACKNOWLEDGMENTS

All images of human volunteers were acquired in accordance with IRB Protocol # 5914E approved by the Boston University Institutional Regulatory Board. We thank Thomas Bifano and the BU Photonics Center for making a Verasonics machine available to us.

REFERENCES

- [1] G. Montaldo, M. Tanter, J. Bercoff, N. Benech, and M. Fink, "Coherent plane-wave compounding for very high frame rate ultrasonography and transient elastography," *IEEE Transactions on Ultrasonics, Ferroelectrics, and Frequency Control*, vol. 56, no. 3, pp. 489–506, Mar. 2009.
- [2] J. Bercoff, G. Montaldo, T. Loupas, D. Saverly, F. Mézière, M. Fink, and M. Tanter, "Ultrafast compound doppler imaging: providing full blood flow characterization," *IEEE Transactions on Ultrasonics, Ferroelectrics, and Frequency Control*, vol. 58, no. 1, pp. 134–147, Jan. 2011, conference Name: IEEE Transactions on Ultrasonics, Ferroelectrics, and Frequency Control.
- [3] J. LONG, G. TRAHEY, and N. BOTTENUS, "SPATIAL COHERENCE IN MEDICAL ULTRASOUND: A REVIEW," *Ultrasound in medicine & biology*, vol. 48, no. 6, pp. 975–996, Jun. 2022. [Online]. Available: <https://www.ncbi.nlm.nih.gov/pmc/articles/PMC9067166/>
- [4] R. Mallart and M. Fink, "The van Cittert–Zernike theorem in pulse echo measurements," *The Journal of the Acoustical Society of America*, vol. 90, no. 5, pp. 2718–2727, Nov. 1991, publisher: Acoustical Society

- of America. [Online]. Available: <http://asa.scitation.org/doi/10.1121/1.401867>
- [5] —, “Adaptive focusing in scattering media through sound-speed inhomogeneities: The van Cittert Zernike approach and focusing criterion,” *The Journal of the Acoustical Society of America*, vol. 96, no. 6, pp. 3721–3732, Dec. 1994, publisher: Acoustical Society of America. [Online]. Available: <http://asa.scitation.org/doi/10.1121/1.410562>
- [6] P.-C. Li and M.-L. Li, “Adaptive imaging using the generalized coherence factor,” *IEEE Transactions on Ultrasonics, Ferroelectrics, and Frequency Control*, vol. 50, no. 2, pp. 128–141, Feb. 2003, conference Name: IEEE Transactions on Ultrasonics, Ferroelectrics, and Frequency Control.
- [7] J. Camacho, M. Parrilla, and C. Fritsch, “Phase Coherence Imaging,” *IEEE Transactions on Ultrasonics, Ferroelectrics, and Frequency Control*, vol. 56, no. 5, pp. 958–974, May 2009, conference Name: IEEE Transactions on Ultrasonics, Ferroelectrics, and Frequency Control.
- [8] K. Hollman, K. Rigby, and M. O’Donnell, “Coherence factor of speckle from a multi-row probe,” in *1999 IEEE Ultrasonics Symposium. Proceedings. International Symposium (Cat. No.99CH37027)*, vol. 2, Oct. 1999, pp. 1257–1260 vol.2, iSSN: 1051-0117.
- [9] M. A. Lediju, G. E. Trahey, B. C. Byram, and J. J. Dahl, “Short-lag spatial coherence of backscattered echoes: imaging characteristics,” *IEEE Transactions on Ultrasonics, Ferroelectrics, and Frequency Control*, vol. 58, no. 7, pp. 1377–1388, Jul. 2011, conference Name: IEEE Transactions on Ultrasonics, Ferroelectrics, and Frequency Control.
- [10] M. A. Lediju Bell, R. Goswami, J. A. Kisslo, J. J. Dahl, and G. E. Trahey, “Short-Lag Spatial Coherence Imaging of Cardiac Ultrasound Data: Initial Clinical Results,” *Ultrasound in Medicine & Biology*, vol. 39, no. 10, pp. 1861–1874, Oct. 2013. [Online]. Available: <http://www.sciencedirect.com/science/article/pii/S0301562913006649>
- [11] G. Matrone, A. S. Savoia, G. Caliano, and G. Magenes, “The Delay Multiply and Sum Beamforming Algorithm in Ultrasound B-Mode Medical Imaging,” *IEEE Transactions on Medical Imaging*, vol. 34, no. 4, pp. 940–949, Apr. 2015, conference Name: IEEE Transactions on Medical Imaging.
- [12] Y. L. Li and J. J. Dahl, “Angular coherence in ultrasound imaging: Theory and applications,” *The Journal of the Acoustical Society of America*, vol. 141, no. 3, pp. 1582–1594, Mar. 2017. [Online]. Available: <https://www.ncbi.nlm.nih.gov/pmc/articles/PMC5390598/>
- [13] C. Yang, J. Xu, Y. Xu, Y. Cui, and Y. Jiao, “Coherent Plane-Wave Compounding Based on United Coherence Factor,” *IEEE Access*, vol. 8, pp. 112 751–112 761, 2020, conference Name: IEEE Access.
- [14] J.-f. Synnevag, A. Austeng, and S. Holm, “Benefits of minimum-variance beamforming in medical ultrasound imaging,” *IEEE Transactions on Ultrasonics, Ferroelectrics, and Frequency Control*, vol. 56, no. 9, pp. 1868–1879, Sep. 2009, conference Name: IEEE Transactions on Ultrasonics, Ferroelectrics, and Frequency Control.
- [15] O. M. H. Rindal and A. Austeng, “Double Adaptive Plane-wave Imaging,” in *2016 IEEE International Ultrasonics Symposium (IUS)*, Sep. 2016, pp. 1–4, iSSN: 1948-5727. [Online]. Available: <https://ieeexplore.ieee.org/document/7728906>
- [16] J. Zhao, Y. Wang, X. Zeng, J. Yu, B. Y. S. Yiu, and A. C. H. Yu, “Plane wave compounding based on a joint transmitting-receiving adaptive beamformer,” *IEEE Transactions on Ultrasonics, Ferroelectrics, and Frequency Control*, vol. 62, no. 8, pp. 1440–1452, Aug. 2015, conference Name: IEEE Transactions on Ultrasonics, Ferroelectrics, and Frequency Control. [Online]. Available: <https://ieeexplore.ieee.org/document/7185011>
- [17] N. Q. Nguyen and R. W. Prager, “A Spatial Coherence Approach to Minimum Variance Beamforming for Plane-Wave Compounding,” *IEEE Transactions on Ultrasonics, Ferroelectrics, and Frequency Control*, vol. 65, no. 4, pp. 522–534, Apr. 2018, conference Name: IEEE Transactions on Ultrasonics, Ferroelectrics, and Frequency Control. [Online]. Available: <https://ieeexplore.ieee.org/abstract/document/8259306>
- [18] S. W. Smith, H. Lopez, and W. J. Bodine, “Frequency independent ultrasound contrast-detail analysis,” *Ultrasound in Medicine & Biology*, vol. 11, no. 3, pp. 467–477, May 1985. [Online]. Available: <https://www.sciencedirect.com/science/article/pii/0301562985901589>
- [19] M. S. Patterson and F. S. Foster, “The Improvement and Quantitative Assessment of B-Mode Images Produced by an Annular Array/Cone Hybrid,” *Ultrasonic Imaging*, vol. 5, no. 3, pp. 195–213, Jul. 1983, publisher: SAGE Publications Inc. [Online]. Available: <https://doi.org/10.1177/016173468300500301>
- [20] S. M. Hverven, O. M. H. Rindal, A. J. Hunter, and A. Austeng, “Point scatterer enhancement in ultrasound by wavelet coefficient shrinkage,” in *2017 IEEE International Ultrasonics Symposium (IUS)*, Sep. 2017, pp. 1–4, iSSN: 1948-5727. [Online]. Available: <https://ieeexplore.ieee.org/document/8092971>
- [21] O. M. H. Rindal, A. Austeng, A. Fatemi, and A. Rodriguez-Molares, “The Effect of Dynamic Range Alterations in the Estimation of Contrast,” *IEEE Transactions on Ultrasonics, Ferroelectrics, and Frequency Control*, vol. 66, no. 7, pp. 1198–1208, Jul. 2019, conference Name: IEEE Transactions on Ultrasonics, Ferroelectrics, and Frequency Control.
- [22] A. Rodriguez-Molares, O. M. H. Rindal, J. D’hooge, S.-E. Måsøy, A. Austeng, M. A. Lediju Bell, and H. Torp, “The Generalized Contrast-to-Noise Ratio: A Formal Definition for Lesion Detectability,” *IEEE Transactions on Ultrasonics, Ferroelectrics, and Frequency Control*, vol. 67, no. 4, pp. 745–759, Apr. 2020, conference Name: IEEE Transactions on Ultrasonics, Ferroelectrics, and Frequency Control.
- [23] O. M. H. Rindal, T. G. Bjåstad, T. Espeland, E. A. R. Berg, and S.-E. Måsøy, “A Very Large Cardiac Channel Data Database (VLCD) Used to Evaluate Global Image Coherence (GIC) as an In Vivo Image Quality Metric,” *IEEE Transactions on Ultrasonics, Ferroelectrics, and Frequency Control*, vol. 70, no. 10, pp. 1295–1307, Oct. 2023, conference Name: IEEE Transactions on Ultrasonics, Ferroelectrics, and Frequency Control.
- [24] J. W. Goodman, *Speckle Phenomena in Optics: Theory and Applications*. Roberts and Company Publishers, 2007, google-Books-ID: TynXEcS0DncC.
- [25] G. Guennebaud, B. Jacob *et al.*, “Eigen v3,” <http://eigen.tuxfamily.org>, 2010.
- [26] D. Garcia, “Make the most of MUST, an open-source Matlab UltraSound Toolbox,” in *2021 IEEE International Ultrasonics Symposium (IUS)*, Sep. 2021, pp. 1–4, iSSN: 1948-5727.
- [27] V. Perrot, M. Polichetti, F. Varray, and D. Garcia, “So you think you can DAS? A viewpoint on delay-and-sum beamforming,” *Ultrasonics*, vol. 111, p. 106309, Mar. 2021. [Online]. Available: <https://www.sciencedirect.com/science/article/pii/S0041624X20302444>
- [28] A. Rodriguez-Molares, O. M. H. Rindal, O. Bernard, A. Nair, M. A. Lediju Bell, H. Liebgott, A. Austeng, and L. Lovstakken, “The UltraSound ToolBox,” in *2017 IEEE International Ultrasonics Symposium (IUS)*, Sep. 2017, pp. 1–4, iSSN: 1948-5727.
- [29] H. Liebgott, A. Rodriguez-Molares, F. Cervenansky, J. Jensen, and O. Bernard, “Plane-Wave Imaging Challenge in Medical Ultrasound,” in *2016 IEEE International Ultrasonics Symposium (IUS)*, Sep. 2016, pp. 1–4, iSSN: 1948-5727.
- [30] J. Albayda and N. van Alfen, “Diagnostic Value of Muscle Ultrasound for Myopathies and Myositis,” *Current Rheumatology Reports*, vol. 22, no. 11, p. 82, Sep. 2020. [Online]. Available: <https://doi.org/10.1007/s11926-020-00947-y>
- [31] C. Yang, Y. Jiao, T. Jiang, Y. Xu, and Y. Cui, “A United Sign Coherence Factor Beamformer for Coherent Plane-Wave Compounding with Improved Contrast,” *Applied Sciences*, vol. 10, no. 7, p. 2250, Jan. 2020, number: 7 Publisher: Multidisciplinary Digital Publishing Institute. [Online]. Available: <https://www.mdpi.com/2076-3417/10/7/2250>
- [32] B. M. Asl and A. Mahloojifar, “Eigenspace-based minimum variance beamforming applied to medical ultrasound imaging,” *IEEE Transactions on Ultrasonics, Ferroelectrics, and Frequency Control*, vol. 57, no. 11, pp. 2381–2390, Nov. 2010, conference Name: IEEE Transactions on Ultrasonics, Ferroelectrics, and Frequency Control.
- [33] Z. Lan, L. Jin, S. Feng, C. Zheng, Z. Han, and H. Peng, “Joint Generalized Coherence Factor and Minimum Variance Beamformer for Synthetic Aperture Ultrasound Imaging,” *IEEE Transactions on Ultrasonics, Ferroelectrics, and Frequency Control*, vol. 68, no. 4, pp. 1167–1183, Apr. 2021, conference Name: IEEE Transactions on Ultrasonics, Ferroelectrics, and Frequency Control.

TABLE I
METHOD AND REFERENCES (PART I)

Method Name	Expression	References
DAS	$B_{\text{das}}(\vec{r}) = \frac{1}{MN} \left(\sum_{m=1}^M \sum_{n=1}^N s_{mn}(\vec{r}) \right)$	[1], [21], [22], [27]
CF	$w_m(\vec{r}) = \frac{ \sum_{n=1}^N s_{mn} ^2}{N \sum_{n=1}^N s_{mn} ^2},$ $B_{\text{CF}}(\vec{r}) = \frac{\sum_{m=1}^M \sum_{n=1}^N w_m s_{mn}}{N}$	[4], [5], [8], [21], [22]
GCF	$w_m(\vec{r}) = \frac{\sum_{n \in L} s_{mn}}{\sum_n s_{mn} ^2},$ $B_{\text{GCF}}(\vec{r}) = \frac{\sum_{m=1}^M \sum_{n=1}^N w_m s_{mn}}{N}$	[6], [21], [22]
PCF	$p_m = \min \{ \sigma(\arg(s_{mn}))_n, \sigma(\arg \text{unwrap}(s_{mn}))_n \},$ $w_m(\vec{r}) = \max \left\{ 0, 1 - \frac{\gamma}{\sigma_0} p_m \right\},$ $B_{\text{PCF}}(\vec{r}) = \frac{\sum_{m=1}^M \sum_{n=1}^N w_m s_{mn}}{N}$	[7], [21], [22]
UCF	$w(\vec{r}) = \frac{ \sum_{m=1}^M \sum_{n=1}^N s_{mn} ^2}{MN \sum_{m=1}^M \sum_{n=1}^N s_{mn} ^2},$ $B_{\text{UCF}} = w \sum_{m=1}^M \sum_{n=1}^N s_{mn}$	[13], [31]
fDMAS	$s_n(\vec{r}) = \sum_{m=1}^M \Re \{ s_{mn}(\vec{r}) \},$ $\hat{s}_n(\vec{r}) = \text{sign}(s_n(\vec{r})) \sqrt{ s_n(\vec{r}) },$ $B_{\text{DMAS}}(\vec{r}) = \sum_{l=1}^L \sum_{n=1}^{N-l} \hat{s}_n(\vec{r}) \hat{s}_{n+l}(\vec{r})$	[11], [21], [22]

Algorithms used for the methods compared in this paper (continued in Table II).

TABLE II
METHODS AND REFERENCES (PART II)

Method Name	Expression	References
MinVar	$s_n(\vec{r}) = \sum_{m=1}^M s_{mn}(\vec{r}),$	
	$\bar{s}_n(\vec{r}) = [s_n(\vec{r}) s_{n+1}(\vec{r}) \cdots s_{n+L-1}(\vec{r})]^T,$	
	$\hat{R}(\vec{r}) = \frac{\sum_{k=-K}^K \sum_{n=0}^{N-L} \bar{s}_n(\vec{r}=(x,z-k)) \bar{s}_n^H(\vec{r}=(x,z-k))}{(2K+1)(N-L+1)},$	[14], [21], [22], [32], [33]
	$\tilde{R}(\vec{r}) = \hat{R}(\vec{r}) + \frac{\Delta}{L} \text{tr}\{\hat{R}(\vec{r})\} I,$	
	$w_{MV}(\vec{r}) = \frac{\tilde{R}^{-1} \vec{a}}{\vec{a}^H \tilde{R}^{-1} \vec{a}},$	
	$B_{MV}(\vec{r}) = \frac{1}{N-L+1} \sum_{l=0}^{N-L} w_{MV}^H(\vec{r}) \bar{s}_n(\vec{r})$	
JCF	$w_{m,n}(x,z) = \frac{\left \sum_{m'=1}^M \sum_{n'=1}^N s_{m',n} s_{m,n'} \right ^\alpha}{(MN)^{\alpha-1} \sum_{m'=1}^M \sum_{n'=1}^N s_{m',n} ^\alpha s_{m,n'} ^\alpha}$	
	$B_{JCF}(x,z) = \frac{1}{MN} \sum_{m=1}^M \sum_{n=1}^N w_{m,n} s_{m,n}$	

Continuation of Table I.